

## Pressure-induced superconductivity in tin sulfide

Ryo Matsumoto,<sup>1,2</sup> Peng Song,<sup>1,2</sup> Shintaro Adachi,<sup>1</sup> Yoshito Saito,<sup>1,2</sup> Hiroshi Hara,<sup>1,2</sup> Aichi Yamashita,<sup>1,2</sup> Kazuki Nakamura,<sup>3</sup> Sayaka Yamamoto,<sup>1,2,3</sup> Hiromi Tanaka,<sup>3</sup> Tetsuo Irifune,<sup>4</sup> Hiroyuki Takeya,<sup>1</sup> and Yoshihiko Takano<sup>1,2</sup>

<sup>1</sup>International Center for Materials Nanoarchitectonics (MANA), National Institute for Materials Science, 1-2-1 Sengen, Tsukuba, Ibaraki 305-0047, Japan

<sup>2</sup>University of Tsukuba, 1-1-1 Tennodai, Tsukuba, Ibaraki 305-8577, Japan

<sup>3</sup>National Institute of Technology, Yonago College, 4448 Hikona, Yonago, Tottori 683-8502, Japan

<sup>4</sup>Geodynamics Research Center, Ehime University, Matsuyama, Ehime 790-8577, Japan



(Received 23 January 2019; revised manuscript received 30 March 2019; published 6 May 2019)

Tin sulfide (SnS) single crystals were synthesized using a melt and slow-cooling method. The obtained crystals were characterized by x-ray diffraction, energy-dispersive spectrometry, and by x-ray photoelectron spectroscopy. Electrical transport properties of SnS were investigated under high pressure using a diamond anvil cell with boron-doped metallic diamond electrodes and an undoped diamond insulating layer. We successfully observed an insulator to metal transition between 8.1 and 12.5 GPa and pressure-induced superconductivity with a transition temperature ( $T_c$ ) of 5.8 K under 47.8 GPa as predicted by theoretical calculations. Comparing with the pressure-induced superconductivity in related SnSe compound, a possible  $T_c$  enhancement in SnS by an increase of density of states at the Fermi level is expected.

DOI: [10.1103/PhysRevB.99.184502](https://doi.org/10.1103/PhysRevB.99.184502)

### I. INTRODUCTION

Tin chalcogenide binary compounds have been studied as superior functional materials with high thermoelectric performance in the past several years [1–7]. Especially, tin selenide (SnSe) shows remarkable thermoelectric property of an ultrahigh figure-of-merit  $ZT$  value of 2.6 at 923 K, due to its low thermal conductivity, controllable resistivity, and high Seebeck coefficient [1,8]. Also, superconductivity in tin selenide was recently reported under high pressure [9]. Tin telluride similarly shows superior thermoelectric property as lead-free materials [10]. The carrier-doped SnTe shows superconductivity around 2 K under ambient pressure [11]. These indicate that tin chalcogenides binary compounds are a new vein of superconducting materials.

According to recent first-principles calculations, superconductivity in tin sulfide binary compounds SnS and Sn<sub>3</sub>S<sub>4</sub> are predicted under high pressure [12]. In the beginning, the stable phase  $\alpha$ -SnS-*Pnma*, at ambient pressure, undergoes a phase transition to a  $\beta$ -SnS-*Cmcm* phase at 15 GPa [13]. Recently, it was reported that this transition from  $\alpha$ -SnS to  $\beta$ -SnS could occur at 9 GPa [12]. Under further compression, an appearance of the  $\gamma$ -SnS-*Pm-3m* phase was experimentally reported under 18 GPa [14]. Recent theoretical calculations suggested that the  $\gamma$ -SnS phase should be stable at 39 GPa exhibiting superconductivity with a transition temperature ( $T_c$ ) of 9.74 K [12]. The higher  $T_c$  compound Sn<sub>3</sub>S<sub>4</sub> (space group *I*-43*d*) shows an instability at ambient pressure. However, the metallic phase is stable at 15 GPa and a maximum  $T_c$  of 21.9 K appears at 30 GPa. Although similar structural transition and superconductivity were experimentally observed in similar compounds, such as SnSe [9] and Sn<sub>3</sub>Se<sub>4</sub> [15], there is no report regarding tin sulfide. Experimental investigation of the high-pressure properties of tin sulfides is an important step for

advancing the physics of chalcogenide binary compounds, including the pressure-induced topological and superconducting phase of SnSe [9]. In this paper, we experimentally confirm the predicted superconductivity in tin sulfide via resistance measurements under high pressure. The observed transport properties were then compared with SnSe.

### II. EXPERIMENTAL

SnS and Sn<sub>3</sub>S<sub>4</sub> single-crystals synthesis was attempted via conventional melt and slow-cooling method. Starting materials of Sn grains (99.99%) and S grains (99.99%) were put into an evacuated quartz tube in stoichiometric compositions of SnS and Sn<sub>3</sub>S<sub>4</sub>. The ampoules were heated at 350 °C for 4 h, then subsequently at 900 °C for 20 h, slowly cooled to 880 °C for 20 h, followed by furnace cooling. The crystal structures of obtained samples were analyzed by x-ray diffraction (XRD) using a Mini Flex 600 (Rigaku) with Cu K $\alpha$  radiation ( $\lambda = 1.5418$  Å). The diffraction peak from Cu K $\alpha_2$  and the background were subtracted from the observed XRD patterns. The compositional ratios were investigated by energy-dispersive spectrometry (EDX) using a JSM-6010LA (JEOL). X-ray photoelectron spectroscopy (XPS) analyses were carried out using an AXIS-ULTRA DLD (Shimadzu/Kratos) with Al K $\alpha$  x-ray radiation ( $h\nu = 1486.6$  eV) to clear the surface states of the obtained crystals. The XPS measurements were operated under a pressure on the order of  $10^{-9}$  Torr. Photoelectron peaks were analyzed by pseudo-Voigt functions peak fitting with a background subtraction by an active Shirley method using the COMPRO software [16]. Superconductivity was examined by electrical transport measurements via a standard four-probe method under high pressure using an originally designed diamond anvil cell (DAC) [17,18]. Cubic boron

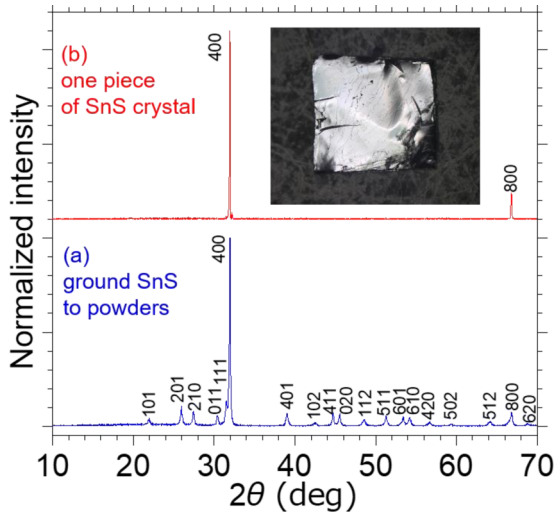


FIG. 1. XRD patterns with Cu  $K\alpha$  radiation ( $\lambda = 1.5418 \text{ \AA}$ ) of (a) ground SnS and (b) a piece of SnS single crystal. The diffraction peak from Cu  $K\alpha_2$  and the background were subtracted from the XRD patterns. The inset shows the optical microscope image for a piece of SnS single crystal.

nitride powders with a ruby manometer were used as a pressure-transmitting medium. Applied pressures were estimated by fluorescence from the ruby powders [19] and by the Raman spectrum from a culet of the top diamond anvil [20] obtained using an inVia Raman Microscope (RENISHAW).

### III. RESULTS AND DISCUSSION

Figure 1(a) shows the powder XRD pattern of ground SnS. All observed peaks were well indexed to an orthorhombic *Pnma* structure. Figure 1(b) exhibits the XRD pattern of a piece of the obtained SnS crystal. An optical microscope image of this piece is shown in the inset. The pattern only exhibits *h*00 diffraction peaks indicating that the sample is a high-quality single crystal. The EDX analysis showed a composition of Sn 52.04% and S 47.96%. The Sn-rich quasistoichiometric composition of SnS is consistent with previous reports [21,22]. On the other hand, the obtained crystals from the  $\text{Sn}_3\text{S}_4$  nominal composition contained only SnS,  $\text{SnS}_2$ , and  $\text{Sn}_2\text{S}_3$  phases. In order to obtain the  $\text{Sn}_3\text{S}_4$  phase, which would show a higher  $T_c$  of 21.9 K according to the theoretical predictions, high-pressure synthesis above 15 GPa should be required [12].

High-resolution XPS measurements of Sn 3*d* orbital were carried out to investigate the surface state of the obtained SnS single crystal. Figure 2(a) shows the Sn 3*d* spectrum of SnS single crystal without cleaving treatment. The spectrum was deconvoluted into four peaks as labeled in Fig. 2(a). The main components of peak 1 at 485.7 eV and peak 2 (centered at 494.1 eV) are corresponding to a  $\text{Sn}^{2+}$  valence state with a spin-orbit splitting of 8.4 eV [23]. The shoulder components of peak 3 (centered at 486.9 eV) and peak 4 (centered at 495.3 eV) are originated from a  $\text{Sn}^{4+}$  oxidation state because of a chemical shift of 0.7–1.5 eV between  $\text{Sn}^{4+}$  and  $\text{Sn}^{2+}$  as accordingly reported by previous studies [24,25].

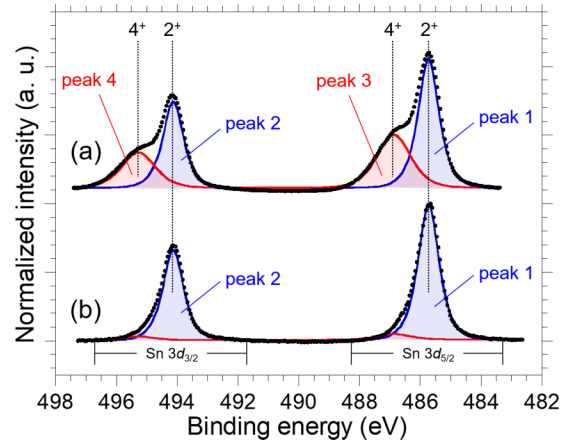


FIG. 2. High-resolution XPS measurements of Sn 3*d* orbital of (a) SnS single crystal without cleaving treatment, and (b) cleaved SnS single crystal in a highly vacuumed prechamber on the order of  $10^{-7}$  Torr using Scotch tape.

Figure 2(b) shows the spectrum from a cleaved SnS single crystal using Scotch tape in a highly vacuumed prechamber on the order of  $10^{-7}$  Torr to obtain its intrinsic valence state. In both Sn 3*d*<sub>5/2</sub> and Sn 3*d*<sub>3/2</sub> orbitals, only sharp peaks were observed at 485.7 and 494.1 eV according to the  $\text{Sn}^{2+}$  state. These results indicate that the outermost surface of SnS is oxidized by air similar to SnSe [26]. Here, the thickness of the  $\text{Sn}^{4+}$  layer was estimated using the equation,  $d = L \cos \theta \ln(I_A/I_B + 1)$  [16], where  $d$  is the thickness,  $L$  is the inelastic mean-free path of a photoelectron from the sample,  $\theta$  is the emission angle,  $I_A$  and  $I_B$  are the peak area intensities from  $\text{Sn}^{4+}$  and  $\text{Sn}^{2+}$  peaks, respectively. The values of  $\theta$  are  $0^\circ$  relative to the sample surface normal,  $L$  is 2.4 nm [27], and  $I_A/I_B$  is 0.63. This estimation indicates that the valence state of  $\text{Sn}^{4+}$  exists within 1.2 nm depth from the surface, while the valence state of the bulk sample is  $\text{Sn}^{2+}$ . Therefore, we can easily evaluate the intrinsic property of SnS by cleaving the sample surface before transport measurements.

Electrical resistivity measurements for the obtained SnS single crystals were carried out at ambient pressure via a standard four-probe method. To prevent surface degradation, we cleaved the sample crystal just before applying the silver paste paint. Figure 3(a) shows a temperature dependence of the resistivity for SnS. The order of resistivity of 50  $\Omega \text{ cm}$  at 300 K is consistent with the typical value of SnS [28]. To evaluate the activation energy of the obtained SnS, the measured resistivity was fitted by the Arrhenius relationship of  $\rho = \rho_0 \times \exp(E_a/k_B T)$ , where  $\rho_0$  is the residual resistivity,  $E_a$  is the activation energy,  $k_B$  is the Boltzmann constant, and  $T$  is the temperature, as shown in the inset of Fig. 3(a). The straight-line fit yields the  $E_a$  value near room temperature of 114 meV. This shallow acceptor level is in agreement with a well-observed tendency in the Sn-rich SnS [29,30].

Figure 3(b) shows a Hall voltage of SnS as a function of the applied magnetic field to confirm the carrier type and concentration at room temperature and ambient pressure. From the slope of Hall voltage versus magnetic field, the carrier concentrations of samples have been calculated using the formula  $(V_H/I) = (1/ned)H$ , where  $V_H$  is the Hall voltage,

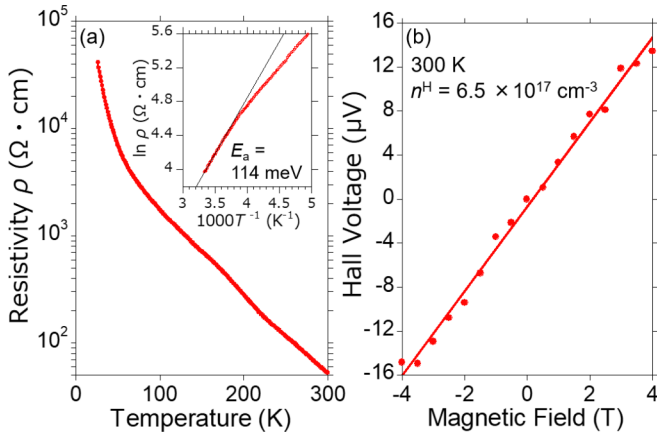


FIG. 3. Transport properties for SnS at ambient pressure. (a) Temperature dependence of resistivity. The inset shows an Arrhenius plot of the resistivity near room temperature. (b) Hall voltage of SnS as a function of applied magnetic field at 300 K.

$I$  is the current,  $n$  is the number of carriers,  $e$  is the elementary charge,  $H$  is the magnetic field, and  $d$  is the sample thickness. The  $V_H$  curve shows a positive slope, indicating a  $p$ -type characteristic with a carrier concentration of  $6.5 \times 10^{17} \text{ cm}^{-3}$ . Although a typical carrier concentration of SnS is on the order of  $10^{15} \text{ cm}^{-3}$  [31], it can be increased up to the order of  $10^{17} \text{ cm}^{-3}$  in the quasioctahedral composition [21], which is consistent with our EDX result. The relatively high carrier concentration would contribute to the observed smaller energy gap in the synthesized SnS.

To examine the predicted superconductivity in SnS, the temperature dependence of resistance was measured under high pressures. Here, we used the originally designed diamond-anvil cell [17,18] for the high-pressure measurements as shown in a schematic image of Fig. 4(a). Sample voltage is detected by heavily boron-doped metallic diamond (BDD) electrodes on the bottom anvil. The electrodes and the metal gasket are electrically separated by an insulating undoped diamond (UDD) layer. The fabrication process details of these special diamonds are described in Refs. [17,18]. In the measurement of SnS, a six-probe design of electrodes was used as shown in Fig. 4(b). Figure 4(c)

is an optical image of a piece of single crystal that was placed on the center of the bottom diamond anvil with the BDD electrodes. The crystal was cleaved by the Scotch tape just before the pressure application to remove any oxidized surface. Since the sample space of DAC was filled by the cBN, the surface degradation of the sample during the high-pressure experiment could be prevented.

Figure 5(a) shows the temperature dependence of the resistance for SnS under pressures up to 47.8 GPa in a log scale. The energy gaps of  $E_g = 2E_a$  as a function of the applied pressure were plotted in Fig. 4(c) via the Arrhenius fitting for the resistance curves as shown in the inset. The sample first shows an insulating behavior under 4 GPa with the energy gap of 0.17 eV which is smaller than that of ambient pressure. The resistance was strongly decreased with applied pressure up to 8.1 GPa. As pressure was increased beyond the theoretically predicted phase boundary of  $\alpha$ -SnS to  $\beta$ -SnS at 9 GPa [12], the sample resistance drastically dropped more than three orders of magnitude in the low-temperature region. This jump in the resistance of SnS could be experimental evidence for the pressure-induced structural transition as predicted by Gonzalez *et al.* [12]. On the other hand, it was found that the energy gap was smoothly decreased with the increase of pressure, with a slope of 16 meV/GPa and extended line approached to zero around 14 GPa. We believe that the metallization in SnS is independent of the structural phase transition.

Figure 5(b) shows the enlarged plot of the temperature dependence of the resistance for SnS around the low-resistance region in linear scale under applied pressure between 18 and 47.8 GPa. The resistance behavior clearly changes under a pressure variation from 18 to 23.6 GPa, which coincides with the experimentally reported phase boundary of  $\alpha$ -SnS to  $\gamma$ -SnS [14]. The compressed SnS exhibited complete metallic tendency under 23.6 GPa with a residual resistance ratio ( $RRR = R_{300\text{K}}/R_{10\text{K}}$ ) of 1.46. After 23.6 GPa there is no change of the resistance behavior up to 43 GPa except for the decrease of  $RRR$ . Under the highest applied pressure of 47.8 GPa, the compressed SnS exhibited a sudden drop of resistance from 5.8 K corresponding to superconducting transition. Under this critical pressure of 47.8 GPa for superconductivity, the shape of the resistance curve in the normal state and the  $RRR$  were almost the same as those of 43 GPa. These

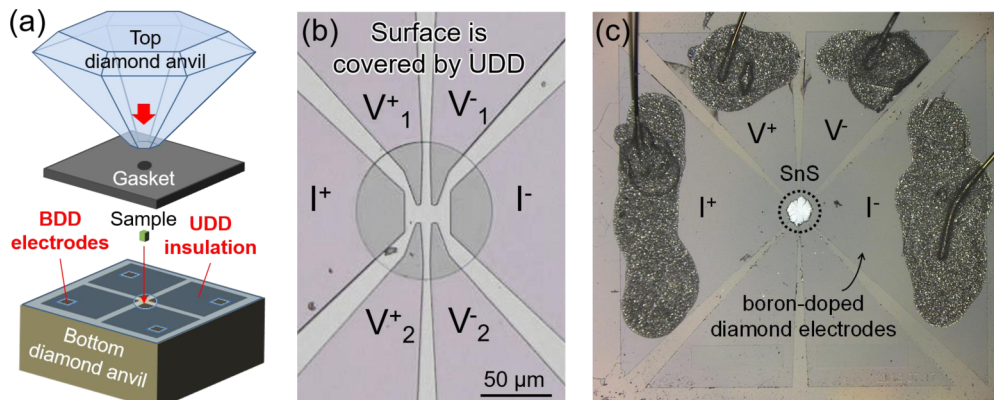


FIG. 4. (a) Originally designed diamond-anvil cell with BDD electrodes and UDD insulating layer. (b) Enlargement of six probe electrodes. (c) Sample space of bottom diamond anvil with one piece of SnS single crystal.



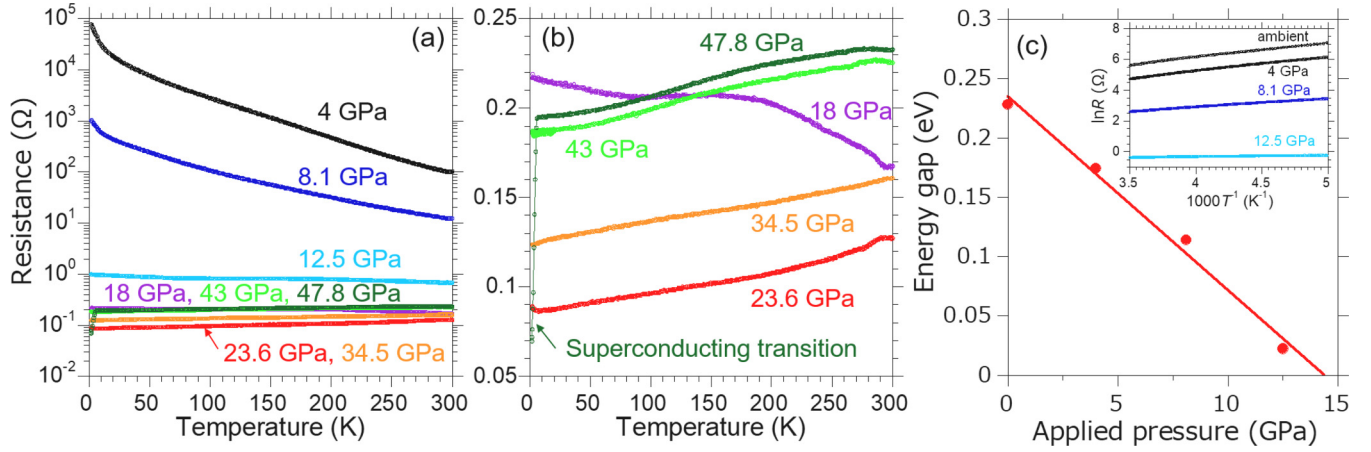


FIG. 5. (a) Temperature dependence of resistance in SnS single crystal under various pressures from 4 to 47.8 GPa in log scale and (b) enlarged plot around low-resistance region in linear scale. (c) Estimated energy gap of SnS as a function of applied pressure. The inset shows Arrhenius plots for resistance under ambient pressure, 4, 8.1, and 12.5 GPa.

results suggest that there is no structural transition between 23.6 and 47.8 GPa. Here we assume that the transition from  $\alpha$ -SnS to  $\beta$ -SnS and  $\beta$ -SnS to  $\gamma$ -SnS occurred around 8.1 and 18 GPa, respectively. Although it is required to conduct *in situ* XRD analysis for more precise determination of the critical pressures of these phase transitions, we first observed the pressure-induced insulator to metal transition and the superconductivity in SnS based on theoretical predictions. The pressure-phase diagram from our experimental measurement of resistance in SnS was concluded in Fig. 6. Due to inhomogeneous pressure distribution in the sample space, sometimes zero resistance could not be observed even when the critical pressure was applied [32]. Although we expected the observation of zero resistance under higher-pressure region, the diamond anvil was broken after the measurement under 47.8 GPa, unfortunately. As a future investigation, further resistance and magnetization measurements will be carried out in order to confirm the zero resistance and Meissner effect, respectively.

To confirm that the drop of resistance in SnS under 47.8 GPa is originated from a superconducting transition, we

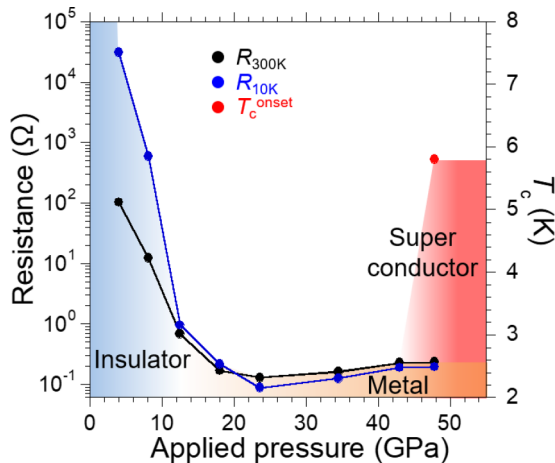


FIG. 6. Pressure-phase diagram from resistance measurement in SnS.

measured the temperature dependence of resistance under magnetic field up to 1.5 T, as shown in Fig. 7(a). The drop of resistance was gradually suppressed by an increase of the applied magnetic field and completely disappeared above 2 K under 1.5 T. This suppression indicates that the drop of resistance in SnS under 47.8 GPa comes from the superconductivity. Figure 7(b) shows a temperature dependence of upper critical field  $H_{c2}$  estimated from the Werthamer-Helfand-Hohenberg (WHH) approximation [33] for type II superconductors in a dirty limit. The extrapolated  $H_{c2}(0)$  was 1.6 T under 47.8 GPa. From the Ginzburg-Landau formula  $H_{c2}(0) = \Phi_0/2\pi\xi(0)^2$ , where  $\Phi_0$  is a fluxoid,  $\xi(0)$  is the coherence length at zero temperature, and the obtained value for  $\xi(0)$  was 1.4 nm.

According to the above investigation, SnS exhibits higher  $T_c$  of 5.8 K than that of superconducting SnSe with *Pm-3m* structure [9]. To discuss the difference in their superconducting properties quantitatively, we additionally synthesized SnSe single crystal and evaluated the high-pressure effect as a comparison. The synthesis conditions were referred to in the literature [8] and details are described in Supplemental Material [34]. In the high-pressure measurements, we used

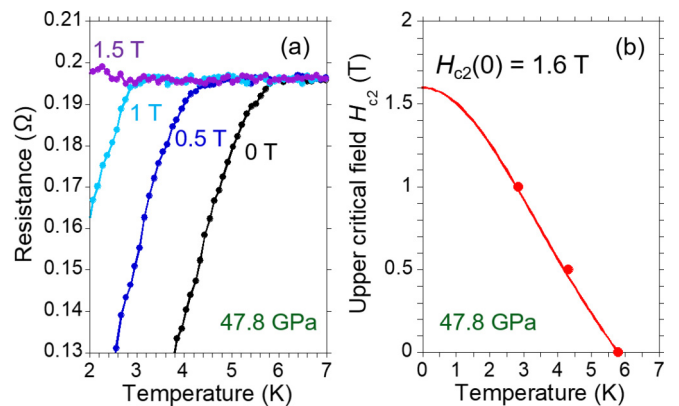


FIG. 7. (a) Temperature dependence of resistance at 47.8 GPa under magnetic field up to 1.5 T. (b) Temperature dependence of upper critical field  $H_{c2}$  estimated from the WHH approximation.

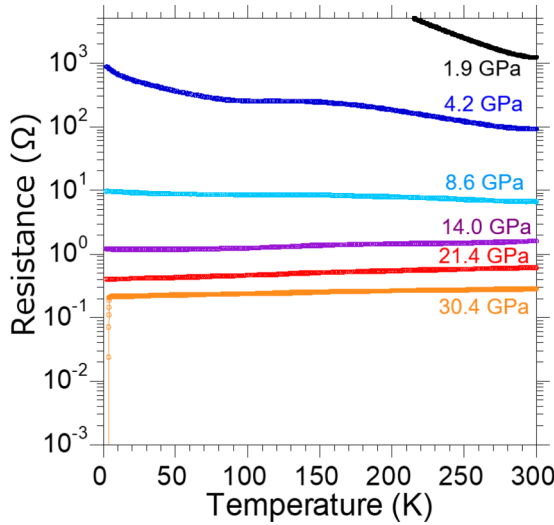


FIG. 8. Temperature dependence of resistance in SnSe single crystal under various pressures from 1.9 to 30.4 GPa in log scale.

the same configuration of DAC with a pressure-transmitting medium of cBN. Figure 8 shows the temperature dependence of the resistance in the SnSe single crystal under pressures ranging from 1.9 GPa to 30.4 GPa in log scale. The insulating behavior of SnSe changed to a metallic character at 14 GPa. Here the critical pressure of metallization for SnSe is in accordance with those of previous reports [9,35]. Upon further compression, the resistance dropped to zero at 30.4 GPa, corresponding to a superconducting transition, with a  $T_c$  of 4.2 K which is 28% lower than that of SnS.

Theoretical studies suggested that there is a possibility of a phonon-mediated Bardeen-Cooper-Schrieffer superconductivity in  $\gamma$ -SnS- $Pm\bar{3}m$  structure [12]. In this case, the  $T_c$  of such a conventional superconductor can be described by the McMillan formula [36]:

$$T_c = \frac{\theta_D}{1.45} \left[ -\frac{1.04(1 + \lambda)}{\lambda - \mu^*(1 + 0.62\lambda)} \right],$$

where  $\lambda$  is the electron-phonon coupling constant and  $\theta_D$  is the Debye temperature. In this formalism,  $\mu^*$  is the Coulomb repulsion parameter, which has typical values between 0.1 and 0.14 [12]. Here, the  $\theta_D$  in metallic materials can be estimated by fitting the temperature dependence of the resistance using the Bloch-Gruneisen equation [37]:

$$R(T) = R_0 + A \left( \frac{T}{\theta_D} \right)^5 \int_0^{\theta_D/T} \frac{x^5}{(e^x - 1)(1 - e^{-x})} dx,$$

where  $R_0$  is the residual resistance,  $A$  is a characteristic constant, and  $T$  is the temperature. Figure 9 shows the temperature dependence of the resistance in (a) SnSe at 30.4 GPa and (b) SnS at 48 GPa. The fitting results for the Bloch-Gruneisen equation are shown by the red solid line. According to the fitting results, the  $\theta_D$  in SnS is 202 K, which is a reasonable value compared to the theoretically calculated phonon frequency value under high pressure [12]. On the other hand, the  $\theta_D$  in SnSe is 92 K which is almost half of that in SnS, reflecting its heavier atomic mass. Consequently, the  $T_c$  of SnS was higher than that of SnSe. Although the  $\theta_D$  for SnSe

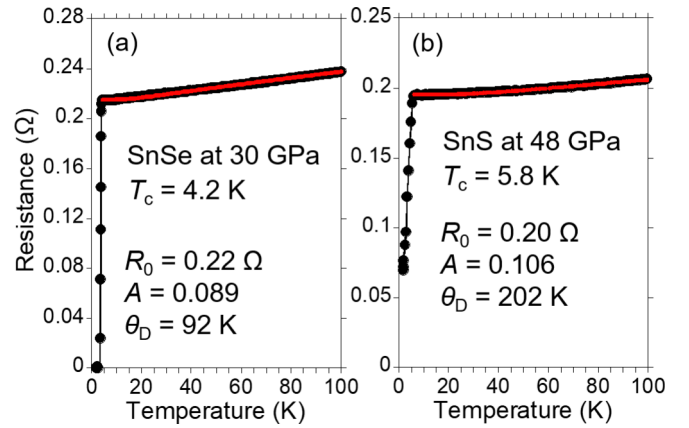


FIG. 9. Temperature dependence of resistance in (a) SnSe at 30.4 GPa and (b) SnS at 48 GPa. The fitting results for the Bloch-Gruneisen equation are shown by the red solid line. The experimental  $T_c$  values, fitting parameters of  $R_0$ ,  $A$ , and  $\theta_D$  are displayed in the figures.

is half of SnS, the  $T_c$  is only 28% lower than that of SnS. This fact indicates that the  $\lambda$ , which is related to the density of state (DOS) at the Fermi level, is higher than that of SnS. A previous work [38] reported that SnSe at ambient pressure shows high DOS near the Fermi level due to its multivalley band structure. By increasing the DOS near the Fermi level in SnS using band-structure engineering techniques such as chemical substitution, defect control and electric field-effect enhancement of  $T_c$  can be expected as future work.

#### IV. CONCLUSION

During this study, we succeeded in the synthesis of SnS single crystal. The resistance measurement under high pressure using our originally designed diamond-anvil cell revealed an insulator to metal transition between 8.1 and 12.5 GPa and superconductivity at 5.8 K under 48 GPa with correspondence to the theoretical prediction. Our experimental observations suggest that the structural transition from  $\alpha$ -SnS to  $\beta$ -SnS and  $\beta$ -SnS to  $\gamma$ -SnS occurred around 8.1 and 18 GPa, respectively. From the comparison with the pressure-induced superconductivity in the related compound SnSe, possible  $T_c$  enhancement in SnS can be achieved by increasing the DOS at the Fermi level using band-structure engineering techniques. Such a theory preceding exploration for superconductors, as for example data-driven approaches [32,39] and the discovery of hydrogen-rich high- $T_c$  superconductors [40–43], is then a promising tool to further accelerate materials science research.

#### ACKNOWLEDGMENTS

The authors thank P. B. Castro for helpful discussions and proofreading of the manuscript. This work was partly supported by JST CREST Grant No. JPMJCR16Q6, JST-Mirai Program Grant No. JPMJMI17A2, and JSPS KAKENHI Grant No. JP17J05926. A part of the fabrication process was supported by NIMS Nanofabrication Platform in Nanotechnology Platform Project sponsored by the Ministry of

Education, Culture, Sports, Science and Technology (MEXT), Japan. Part of the high-pressure experiments were supported

by the Visiting Researcher's Program of Geodynamics Research Center, Ehime University.

- [1] L.-D. Zhao, S.-H. Lo, Y. Zhang, H. Sun, G. Tan, C. Uher, C. Wolverton, V. P. Dravid, and M. G. Kanatzidis, *Nature (London)* **508**, 373 (2014).
- [2] L.-D. Zhao, G. Tan, S. Hao, J. He, Y. Pei, H. Chi, H. Wang, S. Gong, H. Xu, V. P. Dravid, C. Uher, G. J. Snyder, C. Wolverton, and M. G. Kanatzidis, *Science* **351**, 141 (2016).
- [3] Y. Chen, M. D. Nielsen, Y. B. Gao, T. J. Zhu, X. Zhao, and J. P. Heremans, *Adv. Energy Mater.* **2**, 58 (2012).
- [4] E. K. Chere, Q. Zhang, K. Dahal, F. Cao, J. Mao, and Z. Ren, *J. Mater. Chem. A* **4**, 1848 (2016).
- [5] Y.-M. Han, J. Zhao, M. Zhou, X.-X. Jiang, H.-Q. Leng, and L.-F. Li, *J. Mater. Chem. A* **3**, 4555 (2015).
- [6] Q. Tan, L.-D. Zhao, J.-F. Li, C.-F. Wu, T.-R. Wei, Z.-B. Xing, and M. G. Kanatzidis, *J. Mater. Chem. A* **2**, 17302 (2014).
- [7] H. Wu, C. Chang, D. Feng, Y. Xiao, X. Zhang, Y. Pei, L. Zheng, D. Wu, S. Gong, Y. Chen, J. He, M. G. Kanatzidis, and L.-D. Zhao, *Energy Environ. Sci.* **8**, 3298 (2015).
- [8] A. Yamashita, O. Ogiso, R. Matsumoto, M. Tanaka, H. Hara, H. Tanaka, H. Takeya, C. H. Lee, and Y. Takano, *J. Phys. Soc. Jpn.* **87**, 065001 (2018).
- [9] X. Chen, P. Lu, X. Wang, Y. Zhou, C. An, Y. Zhou, C. Xian, H. Gao, Z. Guo, C. Park, B. Hou, K. Peng, X. Zhou, J. Sun, Y. Xiong, Z. Yang, D. Xing, and Y. Zhang, *Phys. Rev. B* **96**, 165123 (2017).
- [10] L. Zhang, J. Wang, Z. Cheng, Q. Sun, Z. Li, and S. Doua, *J. Mater. Chem. A* **4**, 7936 (2016).
- [11] M. Novak, S. Sasaki, M. Kriener, K. Segawa, and Y. Ando, *Phys. Rev. B* **88**, 140502(R) (2013).
- [12] J. M. Gonzalez, K. N. Cong, B. A. Steele, and I. I. Oleynik, *J. Chem. Phys.* **148**, 194701 (2018).
- [13] S. Alptekin and M. Durandurdu, *Solid State Commun.* **150**, 870 (2010).
- [14] L. Ehm, K. Knorr, P. Dera, A. Krimmel, P. Bouvier, and M. Mezouar, *J. Phys.: Condens. Matter* **16**, 3545 (2004).
- [15] H. Yu, W. Lao, L. Wang, K. Li, and Y. Chen, *Phys. Rev. Lett.* **118**, 137002 (2017).
- [16] R. Matsumoto, Y. Nishizawa, N. Kataoka, H. Tanaka, H. Yoshikawa, S. Tanuma, and K. Yoshihara, *J. Electron Spectrosc. Relat. Phenom.* **207**, 55 (2016).
- [17] R. Matsumoto, Y. Sasama, M. Fujioka, T. Irifune, M. Tanaka, T. Yamaguchi, H. Takeya, and Y. Takano, *Rev. Sci. Instrum.* **87**, 076103 (2016).
- [18] R. Matsumoto, A. Yamashita, H. Hara, T. Irifune, S. Adachi, H. Takeya, and Y. Takano, *Appl. Phys. Express* **11**, 053101 (2018).
- [19] G. J. Piermarini, S. Block, J. D. Barnett, and R. A. Forman, *J. Appl. Phys.* **46**, 2774 (1975).
- [20] Y. Akahama and H. Kawamura, *J. Appl. Phys.* **96**, 3748 (2004).
- [21] Yanuar, F. Guastavino, C. Llinares, K. Djessas, and G. Masse, *J. Mater. Sci. Lett.* **19**, 2135 (2000).
- [22] L. A. Burton, D. Colombara, R. D. Abellon, F. C. Grozema, L. M. Peter, T. J. Savenije, G. Dennler, and A. Walsh, *Chem. Mater.* **25**, 4908 (2013).
- [23] J. M. Themlin, M. Chtaib, L. Henrard, P. Lambin, J. Darville, and J. M. Gilles, *Phys. Rev. B* **46**, 2460 (1992).
- [24] J. J. Wang, A. F. Lv, Y. Q. Wang, B. Cui, H. J. Yan, J. S. Hu, W. P. Hu, Y. G. Guo, and L. J. Wan, *Sci. Rep.* **3**, 2613 (2013).
- [25] H. J. Ahn, H. C. Choi, K. W. Park, S. B. Kim, and Y. E. Sung, *J. Phys. Chem. B* **108**, 9815 (2004).
- [26] R. Matsumoto, H. Hara, H. Tanaka, K. Nakamura, N. Kataoka, S. Yamamoto, T. Irifune, A. Yamashita, S. Adachi, H. Takeya, and Y. Takano, *J. Phys. Soc. Jpn.* **87**, 124706 (2018).
- [27] S. Tanuma, S. J. Powell, and D. R. Penn, *Surf. Interface Anal.* **43**, 689 (2011).
- [28] N. K. Reddy and K. T. R. Reddy, *Thin Solid Films* **325**, 4 (1998).
- [29] A. Tanuevski and D. Poelman, *Sol. Energy Mater. Sol. Cells* **80**, 297 (2003).
- [30] M. Ristov, G. Sinadinovski, I. Grozdanov, and M. Mitreski, *Thin Solid Films* **173**, 53 (1989).
- [31] K. T. R. Reddy, N. K. Reddy, and R. W. Miles, *Sol. Energ. Mater. Sol. Cells* **90**, 3041 (2006).
- [32] R. Matsumoto, Z. Hou, M. Nagao, S. Adachi, H. Hara, H. Tanaka, K. Nakamura, R. Murakami, S. Yamamoto, H. Takeya, T. Irifune, K. Terakura, and Y. Takano, *Sci. Technol. Adv. Mater.* **19**, 909 (2018).
- [33] N. R. Werthamer, E. Helfand, and P. C. Hohenberg, *Phys. Rev.* **147**, 295 (1966).
- [34] See Supplemental Material at <http://link.aps.org/supplemental/10.1103/PhysRevB.99.184502> for synthesis procedures of SnSe single crystal.
- [35] J. J. Yan, F. Ke, C. L. Liu, L. Wang, Q. L. Wang, J. K. Zhang, G. H. Li, Y. H. Han, Y. Z. Ma, and C. X. Gao, *Phys. Chem. Chem. Phys.* **18**, 5012 (2016).
- [36] W. L. Mcmillan, *Phys. Rev.* **167**, 331 (1968).
- [37] J. M. Ziman, *Electrons and Phonons: The Theory of Transport Phenomena in Solids*, Oxford Classic Texts in the Physical Sciences (Clarendon, Oxford, 2001).
- [38] T. Nagayama, K. Terashima, T. Wakita, H. Fujiwara, T. Fukura, Y. Yano, K. Ono, H. Kumigashira, O. Ogiso, A. Yamashita, Y. Takano, H. Mori, H. Usui, M. Ochi, K. Kuroki, Y. Muraoka, and T. Yokoya, *Jpn. J. Appl. Phys.* **57**, 010301 (2018).
- [39] R. Matsumoto, Z. Hou, H. Hara, S. Adachi, H. Takeya, T. Irifune, K. Terakura, and Y. Takano, *Appl. Phys. Express* **11**, 093101 (2018).
- [40] A. P. Drozdov, M. I. Erements, I. A. Troyan, V. Ksenofontov, and S. I. Shylin, *Nature (London)* **525**, 73 (2015).
- [41] M. Einaga, M. Sakata, T. Ishikawa, K. Shimizu, M. I. Erements, A. P. Drozdov, I. A. Troyan, N. Hirao, and Y. Ohishi, *Nat. Phys.* **12**, 835 (2016).
- [42] M. Somayazulu, M. Ahart, A. K. Mishra, Z. M. Geballe, M. Baldini, Y. Meng, V. V. Struzhkin, and R. J. Hemley, *Phys. Rev. Lett.* **122**, 027001 (2019).
- [43] A. P. Drozdov, P. P. Kong, V. S. Minkov, S. P. Besedin, M. A. Kuzovnikov, S. Mozaffari, L. Balicas, F. Balakirev, D. Graf, V. B. Prakapenka, E. Greenberg, D. A. Knyazev, M. Tkacz, and M. I. Erements, *arXiv:1812.01561*.